*Journal of Directed Energy*, **1**, Fall 2005, 203–218

# Optical Diagnostics for Pulsed Laser Ablation

**Carl J. Druffner, Patrick D. Kee, Matthew A. Lange, and Glen P. Perram***

*Air Force Institute of Technology, 2950 Hobson Way, Wright–Patterson Air Force Base, Ohio 45433-7765*

**and**

**Rand R. Biggers and Paul N. Barnes**

*Air Force Research Laboratory, Wright–Patterson Air Force Base, Ohio 45433*

*The ablation of target material by pulsed laser deposition (PLD) techniques at high fluence produces highly energetic, ionized plumes with average kinetic energies of more than 50 eV. Optical diagnostics have been developed to monitor the spatial and temporal evolution of the highly nonequilibrium distributions of electronic, vibrational, and translational degrees of freedom. For example, emission time-of-flight profiles have been obtained by using gated imagery to further the development of process control during the pulsed laser deposition of the high-temperature superconductor $YBa_2Cu_3O_{7-x}$. An intensified charge-coupled device (CCD) array was used to obtain a sequence of plume images at 10-ns temporal resolution and 0.2-mm spatial resolution. The resulting streaming speeds of (6–9) $\times$ $10^5$ cm/s and temperatures of 20,000–600,000 K are characterized at selected positions across the full plume. Significant deviations from the forward-directed Maxwellian speed distributions are observed. Ablation plumes are often optically thick, and our recent emission spectroscopy experiments indicate sufficient radiation trapping to observe highly Planckian behavior from neutral and ionized atomic emission lines. Finally, the angular distribution of ejected material is highly forward peaked and fully characterized by high-speed imagery.*

**KEYWORDS:** High-temperature superconductors, PLD, Pulsed laser deposition, YBCO

## 1. Introduction

Pulsed laser deposition (PLD) has become an important method for the production of oriented, high-quality thin films from nanometer to micrometer thicknesses,[4,23] including the reel-to-reel fabrication of meter-to-hundred-meter-length wires coated with the high-temperature superconductor (HTS) $YBa_2Cu_3O_{7-x}$ (YBCO).[5,6,12,16,21,22] High-temperature superconductors carry very high current densities ($>10^6$ A/cm$^2$), allowing high-energy-density power sources and high-magnetic-field applications that are significantly lighter

Received November 10, 2004; revision received February 15, 2005.

*Corresponding author; e-mail: glen.perram@afit.edu.

and more compact than conventional systems.[15] The reduction of weight and size of power systems and magnets enable high-electric-power airborne applications including directed energy weapons.[1,24] In March 2004, SuperPower, a subsidiary of Intermagnetics General Corp., announced the production of a 57-m YBCO HTS wire capable of carrying more than 100 A and then in August 2004 a 100-m-length YBCO-coated conductor.

Full development of the YBCO-coated conductor as the second-generation HTS wire will allow implementation in superconducting generator programs as a replacement for the first-generation Bi-based superconducting wire. This will allow a higher operating temperature with the associated reduction in cooling requirements. In 2003, a 1.5-MVA high-temperature superconducting generator using first-generation wire was built and successfully tested by the General Electric Co. as an engineering prototype for a 100-MVA unit. The HTS coil in the 1.5-MVA demonstrator was designed to operate in the range of 20–40 K and is cooled with a closed-cycle helium refrigeration system employing Gifford–McMahon cryocoolers. GE was just awarded a DOE-SPI contract for the design and development of the 100-MVA HTS generator.

The Air Force is also initiating new HTS generator development programs. As of 2004, Long Electromagnetics (LEI) was constructing an HTS coil test rig or "pseudo generator." These tests will examine HTS field windings at high, >10,000-rpm, rotational speeds, especially as YBCO conductor progresses to the stage of implementation. In October 2004, a major HTS generator program was awarded by the Air Force to GE for construction of a fully operational HTS power generator.

Pulsed laser deposition, as one of the means to achieving long-length YBCO-coated conductors, has many control variables that affect the deposition conditions and quality of the deposited films.[2] In situ monitoring techniques are required to extend the process for repeatable manufacturing of the long lengths (~1 km) of high-quality, defect-minimized superconducting wires necessary for power generation.[3] Many optical techniques for monitoring the energetic gas-phase plume arising from PLD processes have been developed, including time-of-flight (TOF) spectroscopy by using mass spectrometers,[7] ion probes,[8] and emission spectroscopy,[2,3] spectrally resolved visible emission[8–10] and absorption[8] techniques, and fast imagery.[8] Establishing correlations between the plume dynamics and deposited film properties, such as critical current densities and alternate phase inclusions, is an important next step in the development of improved PLD feedback sensors.[2,7]

In this paper, a review of our recent work to develop optical diagnostics for the manufacturing process control of YBCO is provided, including gated intensified charge-coupled device (ICCD) imagery and emission spectroscopy. The imagery is analyzed to provide information regarding the temporal evolution of kinetic energy and angular distributions of individual atomic species within the plume. Important correlations between the angular distributions and observed critical current densities of the deposited YBCO are established. A comprehensive study of the emission spectra establishes electronic state distributions, including the effects of strong optical trapping.

## 2. Experiments

Experiments have been performed in four different laboratories, including collaborations with the Propulsion Directorate and Materials and Manufacturing Directorate of the Air Force Research Laboratory, the Superconducting Technology Center at Los Alamos National Laboratory, and SuperPower, Inc. The experimental apparatus employed in the work

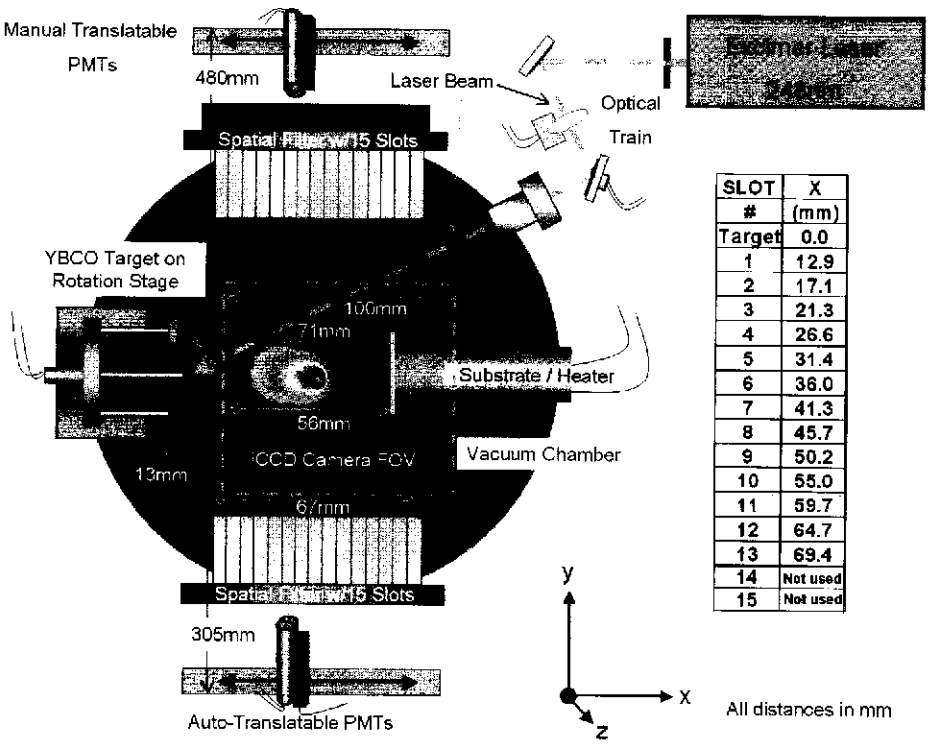


| SLOT # | X (mm) |
|---|---|
| Target | 0.0 |
| 1 | 12.9 |
| 2 | 17.1 |
| 3 | 21.3 |
| 4 | 26.6 |
| 5 | 31.4 |
| 6 | 36.0 |
| 7 | 41.3 |
| 8 | 45.7 |
| 9 | 50.2 |
| 10 | 55.0 |
| 11 | 59.7 |
| 12 | 64.7 |
| 13 | 69.4 |
| 14 | Not used |
| 15 | Not used |

**Fig. 1.** PLD apparatus with imaging and emission TOF sensors.

conducted at the Materials and Manufacturing Directorate is shown schematically in Fig. 1. The apparatus at other locations was conceptually similar, although with the addition of reel-to-reel manufacturing capability.

The pulsed laser deposition apparatus was described in detail previously.[2,3] A Lambda Physik LPX 305i excimer laser provides a ~350–450 mJ ($5.7 \times 10^7$–$8.7 \times 10^7$ W/cm$^2$ per pulse at target), 17-ns pulse at $\lambda = 248$ nm deposited in a $\Delta x \cong 2.2$ mm $\times$ $\Delta y \cong 15$ mm spot typically at a 4-Hz repetition rate. The laser energy is delivered to a rotating tetragonal-YBCO target at 45 deg via aperture, turning mirror, and two-axis scanning mirror. The 38-cm (15-in.)-diameter deposition chamber contains a substrate heater assembly ($\leq$900°C), pressure control for $10^{-5}$–1-torr oxygen background gas (50–600 mtorr in the present study), and 15-cm (6-in.) fused quartz windows on both photo multiplier tube (PMT) sides, and a 20-cm (8-in.) Pyrex window on top.

The geometry for both the fast imagery and scanned PMT emission sensors is illustrated in Fig. 1. A Princeton Instruments PI-Max intensified $512 \times 512$ CCD array with f/1.4 lens was used to image the plume from above (+$z$ direction). The camera was located at 520 mm above the plume centerline, with a field of view of $100 \times 100$ mm (0.2 mm/pixel). The view included the substrate heater, but the target is recessed in a port area extension tube and is obscured for the first 10 mm from the target. The cross-plume ($y$) view is sufficient to capture the full plume. The depth of field for the f/1.4 lens was about 6 mm, which significantly weights the center of the plume. The camera was gated (10 ns) with an ST-133 controller triggered by a photodiode observing the laser pulse. The temporally

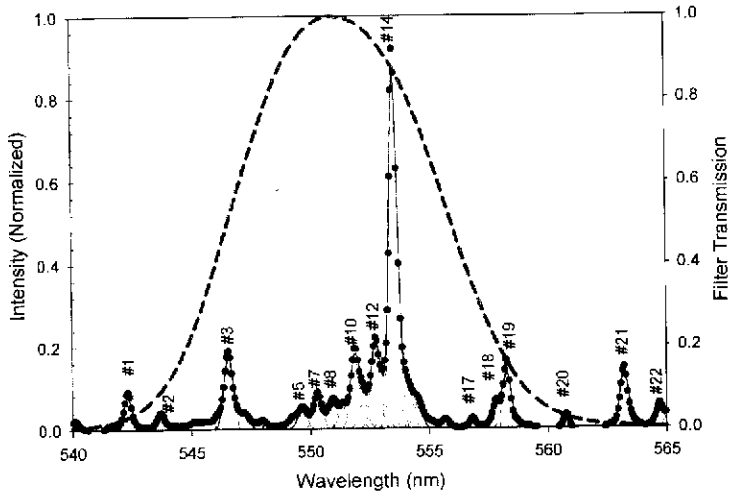


**Fig. 2.** Emission spectra over Ba I filter near 550 nm. Labeled lines are described in Table 1.

evolving plume was monitored by increasing the delay between laser trigger and the camera gate.

Four Hamamatsu R74004-04 PMTs are used to monitor the TOF emission from both sides of the chamber and can be translated across 15 slots, which act as spatial filters. The slots are each 4 mm wide × 60 mm long and located in the vacuum chamber just inside the fused quartz windows. The full width of the slot assembly is 72 mm, with the first slot located at 13 mm from the target, and the 13th slot centered about 2 mm in front of the substrate. The final two slots are not used in the current distance deposition.

Figure 1 provides the distance from the target to the center of each slot. Further spatial filtering is provided by placing each PMT in a 90-mm (or 200-mm)-long × 15 mm diameter cylinder with a 1-mm slit on the chamber end. The pair of PMTs is located 300 and 458 mm from the chamber center line, with the difference attributed to a longer window arm on one side.

For the emission spectroscopy experiments, a fiber probe with focusing input lens was located at one of two locations: 1) from above in place of the ICCD camera or 2) from the side, replacing one of the two translatable PMT sensors.

Band-pass filters were employed with both the ICCD camera and PMT sensors to emphasize the emission from one of the atomic species. In Fig. 2, a moderate-resolution (0.4-nm) spectrum of the plume with strong neutral atomic barium emission is shown with spectral features assigned in Table I. The band-pass filter's spectral response is also displayed, allowing for an assessment of the fraction of the transmitted emission due to neutral atomic barium. The most intense feature is assigned to the Ba $I\ ^1S_o \leftarrow {}^1P^o_1$ transition, which terminates on the ground state and therefore is significantly affected by radiation trapping.[20] Of the 23 most intense, relevant atomic lines in this region,[19] only one, the weak Y $I\ ^2F_{5/2} \leftarrow {}^4D^o_{7/2}$, is not observed. In equilibrium at $T = 6{,}000$ K, this line would be only 0.011 as intense as the prominent Ba $I\ ^1S_o \leftarrow {}^1P^o_1$ line. A fit of the observed spectrum to the set of 24 lines of Table I with a common Gaussian line shape [0.428 nm, full width at half-maximum (FWHM)] is also shown in Fig. 2. The resulting line intensities and 62% peak transmission of the filter yields the fraction of emission due to neutral atomic barium

**Table 1.** Atomic emissions transmitted by band-pass filter

| Peak | Emitter | Assignment | Intensity | % of signal |
|---|---|---|---|---|
| 1 | Ba I | $^3P^\circ_0 \leftarrow {}^3D_1$ | $2.73 \pm 0.21$ | 0.1 |
| 2 | Y I | $^2F_{7/2} \leftarrow {}^2D_{5/2}$ | $1.07 \pm 0.21$ | 0.2 |
| 3 | Y I | $^4F_{9/2} \leftarrow {}^4G_{11/2}$ | $5.46 \pm 0.50$ | 4.3 |
| 4 | Y I | $^2F_{5/2} \leftarrow {}^2F^\circ_{5/2}$ | $1.31 \pm 0.68$ | 1.1 |
| 5 | Y II | $^3P_1 \leftarrow {}^3P^\circ_2$ | $1.46 \pm 0.22$ | 1.5 |
| 6 | Y II | $^3P_2 \leftarrow {}^3P^\circ_2$ | $1.73 \pm 0.21$ | 2.7 |
| 7 | Y I | $^2F_{7/2} \leftarrow {}^2F^\circ_{7/2}$ | $2.86 \pm 0.21$ | 4.6 |
| 8 | Y II | $^3F_2 \leftarrow {}^1D^\circ_2$ | $2.23 \pm 0.28$ | 3.6 |
| 9 | Y I | $^4P_{5/2} \leftarrow {}^4F^\circ_{5/2}$ | $1.77 \pm 0.28$ | 2.9 |
| 10 | Ba I | $^3P^\circ_1 \leftarrow {}^3D_2$ | $6.00 \pm 0.47$ | 9.6 |
| 11 | Y I | $^2F_{5/2} \leftarrow {}^2G^\circ_{7/2}$ | $2.27 \pm 0.46$ | 3.6 |
| 12 | Y I | $^4F_{7/2} \leftarrow {}^4G^\circ_{9/2}$ | $7.33 \pm 0.49$ | 11.2 |
| 13 | Y I | $^2P_{3/2} \leftarrow {}^4P^\circ_{5/2}$ | $2.01 \pm 0.48$ | 3.0 |
| 14 | Ba I | $^1S_0 \leftarrow 1P^\circ_1$ | $29.94 \pm 0.29$ | 42.2 |
| 15 | — | — | $3.47 \pm 0.30$ | 4.6 |
| 16 | Y I | $^2F_{5/2} \leftarrow {}^4D^\circ_{5/2}$ | $2.15 \pm 0.33$ | 2.6 |
| 17 | Y I | $^4P_{5/2} \leftarrow {}^2G^\circ_{7/2}$ | $0.67 \pm 0.21$ | 0.4 |
| 18 | Y I | $^2F_{3/2} \leftarrow {}^2G^\circ_{9/2}$ | $1.97 \pm 0.26$ | 0.7 |
| 19 | Y I | $^4F_{5/2} \leftarrow {}^4G^\circ_{7/2}$ | $4.60 \pm 0.26$ | 1.2 |
| 20 | Y I | $^4F_{9/2} \leftarrow {}^4G^\circ_{9/2}$ | $0.76 \pm 0.21$ | 0.0 |
| 21 | Y I | $^2F_{7/2} \leftarrow {}^4D^\circ_{7/2}$ | $4.68 \pm 0.21$ | 0.0 |
| 22 | Ba I | $^1P^\circ_1 \leftarrow {}^3D_2$ | $1.66 \pm 0.28$ | 0.0 |
| 23 | Y I | $^2D^\circ_{5/2} \leftarrow {}^4D_{7/2}$ | $1.03 \pm 0.28$ | 0.0 |
| 24 | Ba I | $^1P^\circ_1 \leftarrow {}^3D_1$ | $3.33 \pm 0.21$ | 0.0 |

as about 52%, which depends (~5% variance) on the deposition condition. Similar filters were employed for neutral and singly ionized Y and Cu emissions.

## 3. Results

### 3.1. TOF profiles and kinetic energy distributions

TOF diagnostics are particularly useful in characterizing the kinetic energy distributions of various plume constituents and can be used as a deposition control parameter.[2,4] The plumes exhibit high kinetic energies (~50 eV), and the oxygen background gas (~200 mtorr) serves to thermalize the plume over distances of 1–20 cm (Ref. 8). TOF spectroscopy usually involves monitoring the flux (or concentration) of some specie(s) at a specified distance from the target as a function of time. Mass spectrometry and fast Langmuir probes are typically used to monitor the significant ionic content of the plume.[4] Neutral species are monitored by emission with spectrally filtered photodiodes or PMTs,[2,3] or by laser absorption[18,26] or laser-induced fluorescence[10,15,18] techniques for ground states. Typically, the detector's collection volume provides a spatial resolution of $\geq 1$ mm. Translating the detector is required to monitor different locations within the plume.

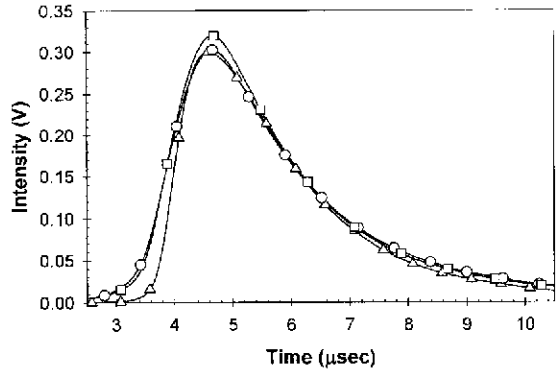


**Fig. 3.** Averaged TOF profiles recorded from three PMT sensors: □, PMT 2; ○, PMT 3; and △, PMT 4, viewing the same volume at $x = 3.6$ cm for 200-mtorr oxygen. More than 4,000 time samples are represented by the solid line. Symbols are added only for identification.

Fast plume imagery using gated ICCD arrays have previously been used to characterize the fluid dynamic effects, shock structure, and reactive scattering of PLD plumes.[4,8] In the present work, a noninvasive emission TOF technique is developed based on such fast plume imagery that provides a high-resolution spatial map of the TOF spectra. By comparing the ICCD imaging and scanned PMT emission TOF techniques, an assessment of the effects of spatial resolution on observed kinetic energy distributions is attained. Issues associated with pulse-to-pulse variations and longer-term temporal drift in PLD TOF measurements are also addressed. Finally, the power of the imaging technique is demonstrated by establishing the dynamics of the kinetic energy distributions. Deviations from the forward-directed Maxwellian distributions typically used to characterize PLD TOF spectra are clearly demonstrated.

Typical TOF spectra observed by the PMTs in these YBCO depositions exhibit ablated atom kinetic energies of ~50 eV and energy distributions with widths of ~5–20 eV, as shown in Fig. 3. During well-controlled depositions, where the peak in the TOF spectra is used as a control parameter,[2,3] the repetitive TOF spectra from an individual PMT exhibit less than 1% deviation in peak time but typically 8% in width and 6% in amplitude over a collection time of several minutes. This variability is significantly reduced when TOF spectra from multiple laser pulses are averaged. Figure 3 illustrates the TOF spectra for an average of 640 laser shots for three PMTs viewing the same target distance. Note that viewing volume discrepancies can be easily introduced when attempting to aim multiple PMTs at the same chamber position or when trying to relocate a translatable sensor. In Fig. 3, a 17% variation in TOF width and 2% TOF peak time are observed for two PMTs located on top of one another on one side of the chamber and a third PMT located on the opposite side of the chamber. Clearly, the systematic errors in these TOF spectra are larger than the low statistical uncertainties.

The intensified CCD movies capture all the information necessary to obtain emission TOF spectra for all locations within the plume simultaneously. A sequence of several barium-filtered (552.5-nm) images for a 200-mtorr deposition is shown in the contour plots of Fig. 4. The plume emission reaches the substrate at ~12.5 $\mu$s, with a significant decrease

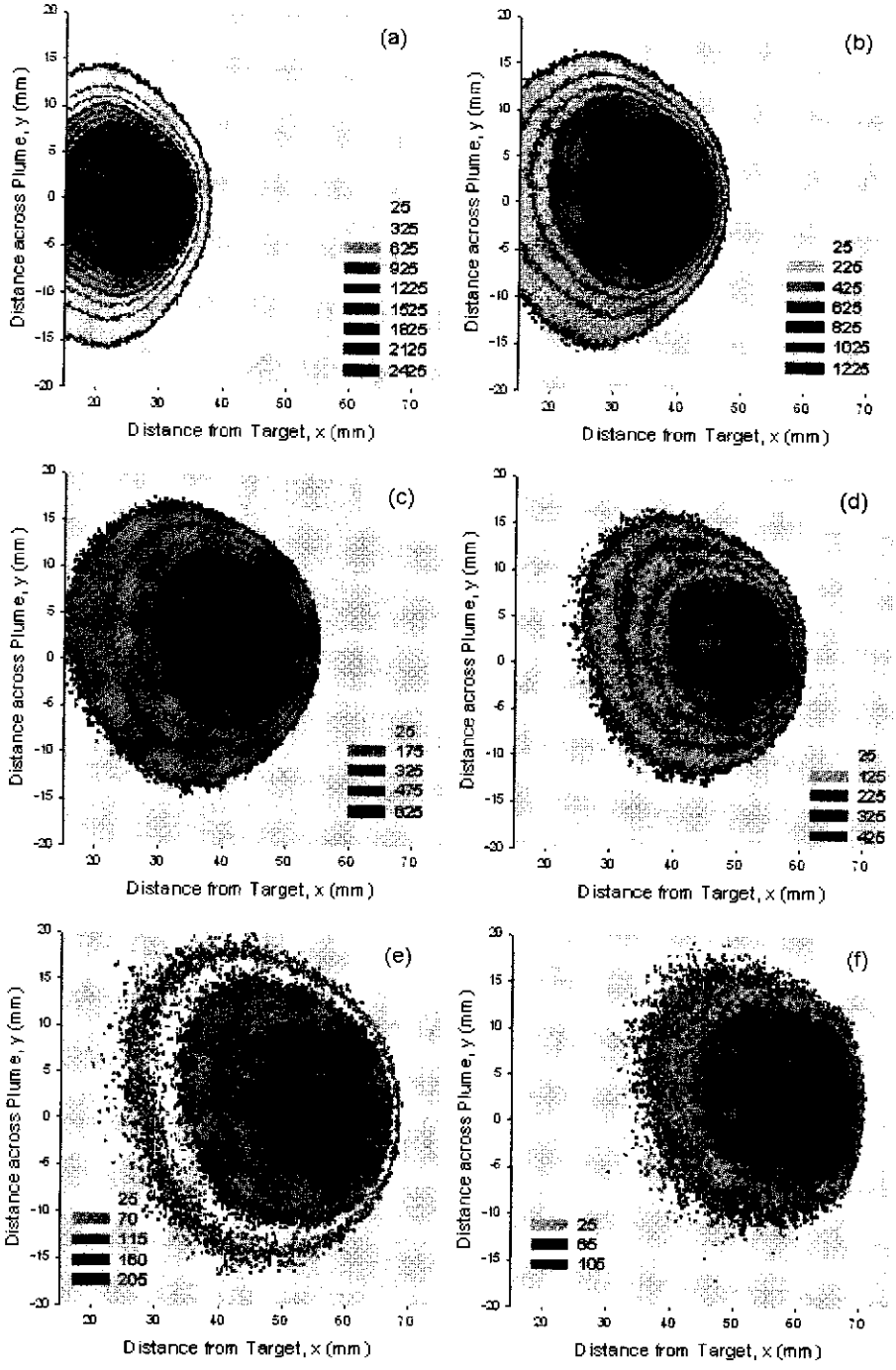


**Fig. 4.** Sequence of ICCD images at $\lambda = 552.5$ nm captured at time delays of 3, 5, 7, 9, 11, and 13 $\mu$s (panels a, b, c, d, e, and f, respectively) after ablation. Gray-scale levels indicate ICCD intensity in counts.

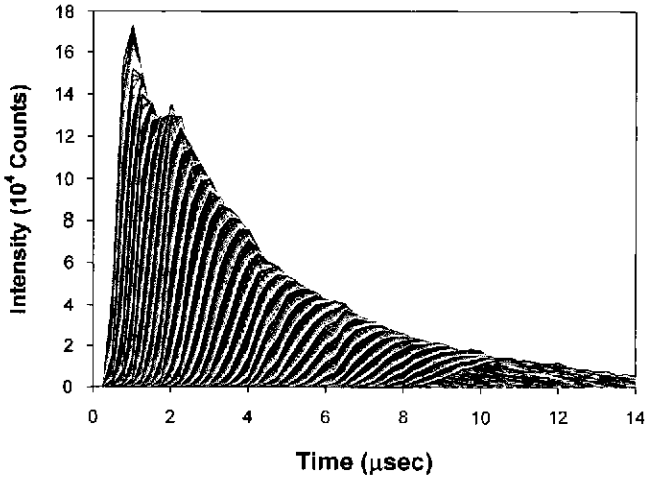


**Fig. 5.** TOF profiles corresponding to the data from Fig. 4, adjusted for both jitter and flicker.

in emission intensity as the plume propagates. The expansion Mach number increases to $M \sim 5$, and the plume is highly forward peak, as discussed below.

To obtain emission TOF spectra from the imagery, the intensities for all CCD pixels with a constant distance to the target (the row, $x =$ constant) are summed. This summed intensity for multiple image frames provides the temporal evolution necessary to construct the TOF spectrum, as shown in Fig. 5. An extensive series of TOF spectra for 125 different chamber distances of 29–54 mm are obtained with a spatial resolution of about 0.2 mm. However, the spectra suffer from both jitter and flicker associated with pulse-to-pulse variation in the plumes. Intensity variations up to 20% (flicker) and sudden shifts in plume center-of-mass (jitter) of up to 3 mm are observed. Two physically based methods for averaging these fluctuations have been developed and applied to TOF spectra provided in Fig. 5.

TOF data are often represented by a modified Maxwell–Boltzmann distribution with a forward-directed (center-of-mass shifted) streaming speed[4,25]:

$$f(v) = A(m/2\pi k)^{\frac{3}{2}} v^n e^{-m(v-u)^2/2kT}\, dv, \tag{1}$$

where $m =$ mass of the emitter, $k =$ Boltzmann constant, $v =$ speed (along propagation direction $x$), $u =$ streaming speed, $T =$ stream temperature describing the width of the speed distribution, and $n =$ integer exponent, typically 3.

Typically, PLD of YBCO yields forward-directed speeds of $u \sim 10^6$ cm/s (Refs. 4, 7, 10, and 17) and speed distributions characterized by temperatures of up to $T \leq 35{,}000$ K (Ref. 18). Results depend significantly on laser energy, laser spot size, detector location, and background gas pressure. Usually, the TOF data are limited to a few fixed locations within the plume and the evolution of the distribution as the plume propagates away from the target is not explored.

A thorough examination of the evolution of the TOF profiles and kinetic energy distributions as the plume propagates from the target to the substrate is enabled by the imagery-based TOF data. The results of fitting Eq. (1) to the TOF profiles for all target distances $x$ are

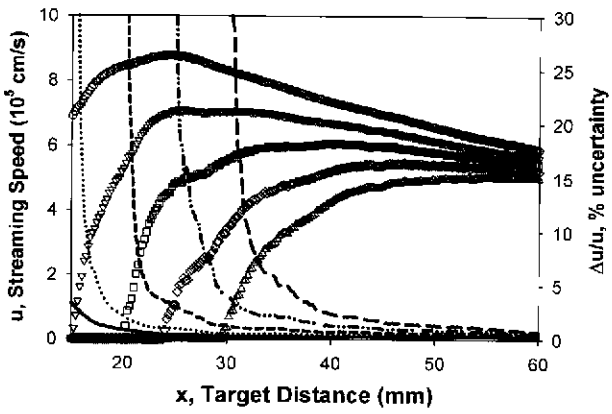


**Fig. 6.** Streaming speeds $u$ for various values of $n = 0$ (○), 1 (▽), 2 (□), 3 (◇), and 4 (△), as the plume propagates from the target. The corresponding percent uncertainty in the fit streaming speed is provided for $n = 0$ (—), 1 (· · ·), 2 (- - -), 3 (-·-·-), and 4 (– –).

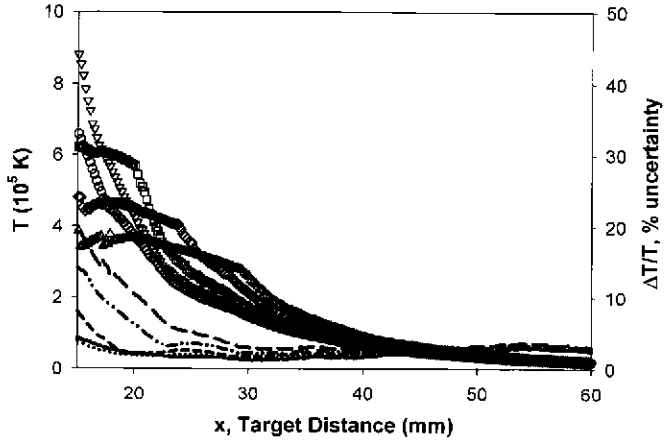


**Fig. 7.** Temperature $T$ for various values of $n = 0$ (○), 1 (▽), 2 (□), 3 (◇), and 4 (△) as the plume propagates from the target. The corresponding percent uncertainty in the fit temperature is provided for $n = 0$ (—), 1 (· · ·), 2 (- - -), 3 (-·-·-), and 4 (– –).

provided in Figs. 6 and 7. There is a systematic variation in fit residual and the extracted speeds $u$ and temperatures $T$, depending on the exponent $n$. Very poor fits are realized for the higher values of $n$, particularly near the target. Considerable discussion regarding the theoretically appropriate value for $n$ is found in previous literature.[13,14,18,25,26]

The modified Maxwellian distribution of Eq. (1) assumes that the speed distribution has equilibrated after propagating a short distance from the ablated target and that signal is a direct measure of the concentration of the indicated specie. Emission TOF profiles monitor the concentration of excited (emitting) states. The collisional processes by which the electronically excited atoms are produced also depend on the cross sections as a function of relative kinetic energy. If the collision energy is significantly above threshold (easily satisfied in PLD) and the additional reagent channels are not accessible (poorly satisfied in

PLD systems, where many excited states, oxide products, etc., are accessible), then a weak dependence of excitation rate on relative speed might be expected. However, TOF profiles for ground-state species obtained by absorption or laser-induced fluorescence techniques differ significantly from the emission TOF profiles recorded under the same conditions.[10] Also note that the emission TOF sensor monitors the intensity from several excited states of both Ba and Y, which may have different speed distributions.

A-well established shock front and speed distribution is expected for target distances greater than about 1 cm for oxygen pressures of 200 mtorr (Ref. 7). Figure 7 indicates that the $n = 3$ distribution is not satisfactory until the plume propagates to targets distances of at least 4 cm. In this region, the shape of the TOF profile is insensitive to the integer exponent, but the extracted streaming speed and temperature are systematically biased with $n$. Complete physical interpretation of the fit parameters is problematic. However, the use of profiles with $n = 0$ appears to produce the best description for all locations in the plume.

Very high streaming temperatures, $T \sim 600{,}000$ K, are observed near the target. Even at $x = 5$ cm the temperatures are ~40,000 K. It is important to note that these streaming temperatures represent the width of the forward-directed speed distribution function. For a TOF profile, $f(t)$, which propagates without change in streaming speed or temperature, the width of the profile increases at larger target distances, but the ratio of the width to the most probable time is a constant. At $T = 600{,}000$ K ($kT = 52$ eV), the profile width nearly equals the peak time. Temperatures as high as $T = 350{,}000$ have been reported at target distances as great as 72 mm (Ref. 25).

There appears to be an acceleration of the plume ($du/dx > 0$) near the target, even for the $n = 0$ profiles. It is possible that this apparent acceleration is an artifact of the chosen distribution function. Alternatively, if the source of emission involves electron impact or ion recombination, then it is conceivable that the plume does accelerate in this region surrounding the target. Another possible source for the plume acceleration is interaction of the expanding plume with the laser beam[11] or by the electric field in a plasma state caused by a difference in velocity between the electrons and ions.[7] Further examination of the dynamics of the kinetic energy distributions is warranted and enabled by the new imaging TOF instrumentation.

### 3.2. Angular distributions and correlations with deposited film critical currents

The camera images contain a wealth of dynamic data about the plume evolution. The expansion Mach number[25] provides a measure of shock strength:

$$M_{\text{exp}} = \sqrt{mu^2/\gamma kT}, \tag{2}$$

where $\gamma$ is the specific heat ratio, $k$ is the Boltzmann constant, $m$ is the mass of the plume, $u$ is the streaming velocity extracted from the TOF data, and $T$ is the temperature describing the velocity spread calculated from the modified Maxwell–Boltzmann. The expansion Mach number typically increases to $M \sim 5$ as the plume propagates across the chamber.

The plume is highly forward peaked with an angular distribution adequately described by

$$g(\theta) = B\cos^m(\theta) + c,$$
$$\theta = \tan^{-1}(y/x), \tag{3}$$

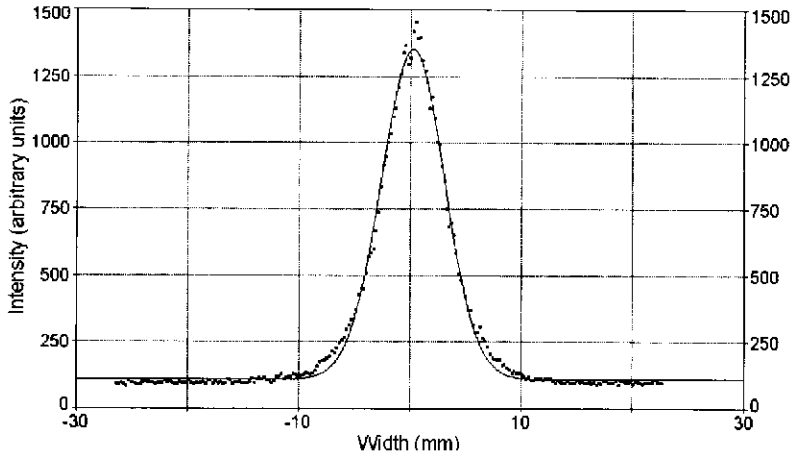


**Fig. 8.** Observed Ba plume intensity (●) and fit (—) to Eq. (3) at 8 $\mu$s after ablation for 200-mtorr oxygen background pressure. The degree of forward peaking is $n = 143 \pm 1.85$.

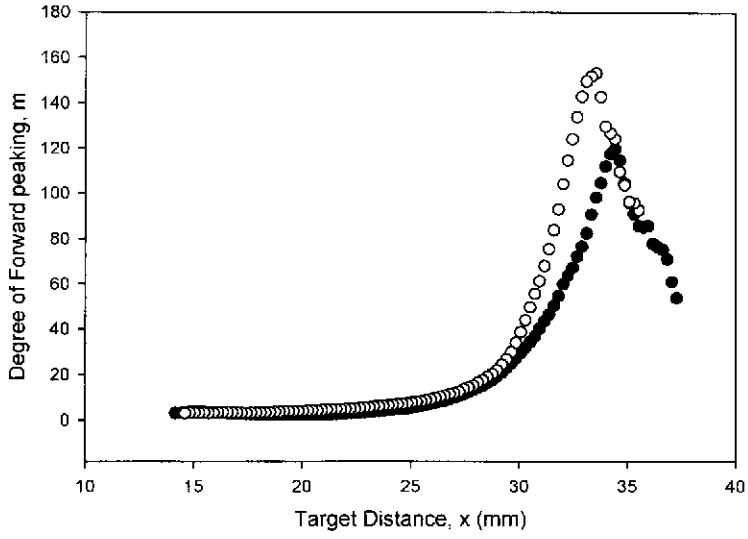


**Fig. 9.** Degree of forward peaking $m$ as a function of position $z$ for ●, Ba and ○, Cu, collected at 200 mtorr and 650 mJ.

with $m = 0$–300, again depending on distance from the target. A typical angular distribution and fit to Eq. (3) is shown in Fig. 8. The angular distributions also depend significantly on atomic specie, as illustrated in Fig. 9.

The difference in angular distribution is highly correlated with the quality of deposited YBCO films. In Fig. 10, the critical currents of different deposited YBCO films are shown, correlated with the difference in angular plume cosine power $m$ for the neutral barium and copper emissions. A wide range of deposition conditions is represented in Fig. 10, indicating the merit of this correlation. To further explore the potential of the signature for process control, the variability in this $\Delta m$ parameter was studied under PLD conditions

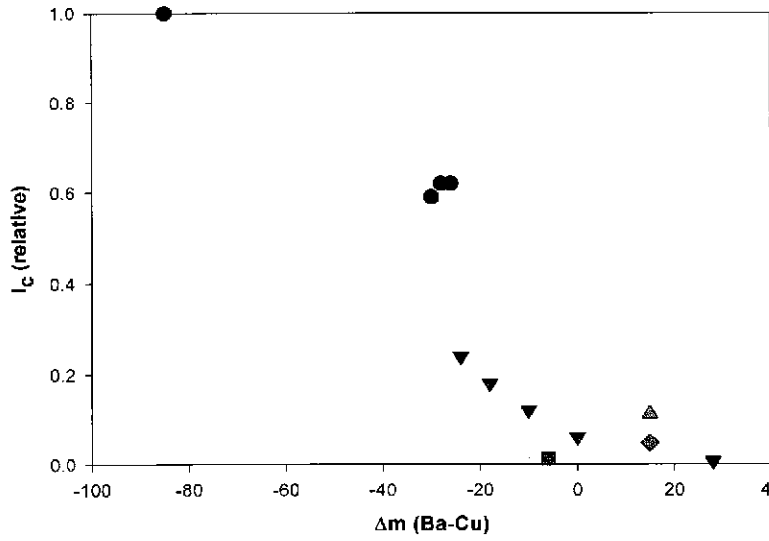


**Fig. 10.** Correlation between deposited critical currents and the difference in degree of forward peaking $m$ for barium and copper plume emissions: ●, 400 mtorr looking from the side; ▽, 200 mtorr (side); □, 100 mtorr (front); ◇, 200 mtorr (front); and △, 300 mtorr (front).

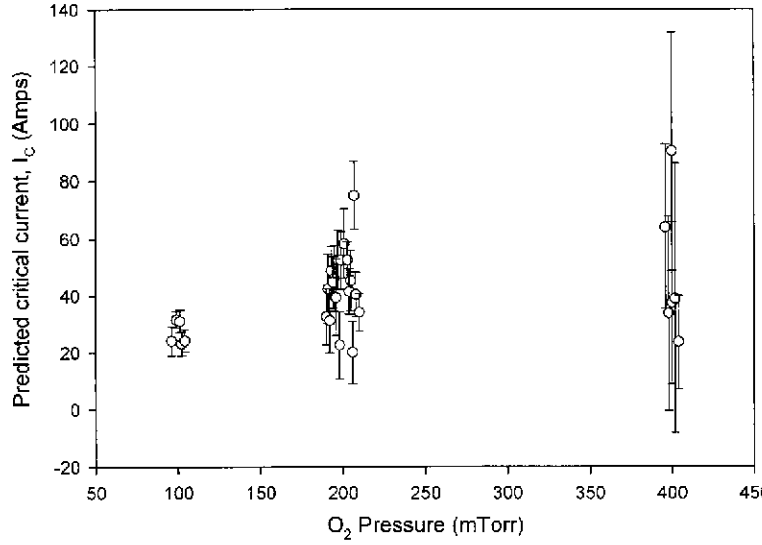


**Fig. 11.** Predicted critical currents based on correlation presented in Fig. 9. The difference in barium and copper angular distributions is shown for three chamber pressures and a laser energy of 650 mJ.

that were intended to be constant. Considerable variability in plume conditions is observed in the results of Fig. 11. However, after data analysis an equipment evaluation showed that operational issues with the laser's optical train were present for this chamber and after correction the operators reported much better film deposition. It is not known whether the

large deviation in the sample was directly attributable to the optical train issue with the chamber. The error bars for each data point represent the standard deviation in 10 images for plumes acquired in rapid succession. The cluster of data points at each deposition condition represent additional sets of 10 images acquired throughout the day on each of the two test days. Indeed, controlling depositions based on specie-dependent angular distributions appears promising. However, the correlation requires further study under controlled deposition conditions.

### 3.3. Emission spectra and electronic state distributions

Plume emission spectra have been recorded across the visible range at 0.4-nm resolution at a variety of deposition conditions and target distances. A segment of a typical spectrum is shown in Fig. 12. Assuming that the plume does not reabsorb emitted photons, the observed intensities for a transition from state $i$ to state $j$, $I(\lambda_{ij})$ are proportional to the concentration of the emitter:

$$I(\lambda_{ij}) = \kappa(\lambda) N_i A_{ij}, \tag{4}$$

where $v_{ij} = c/\lambda_{ij} = (E_i - E_j)/h$, $E_i$ = energy of the $i$th state, $A_{ij}$ = spontaneous emission rate for transition from emitting state $i$ to final state $j$, and $\kappa(\lambda)$ = proportionality constant depending on spectral response of the spectrometer.

The resulting electronic state distribution $N_i$ may be statistically distributed:

$$N_i/N_0 = (g_i/g_o)e^{-(E_i - E_o)/kT_e}, \tag{5}$$

where $g_i$ is the degeneracy of state $i$.

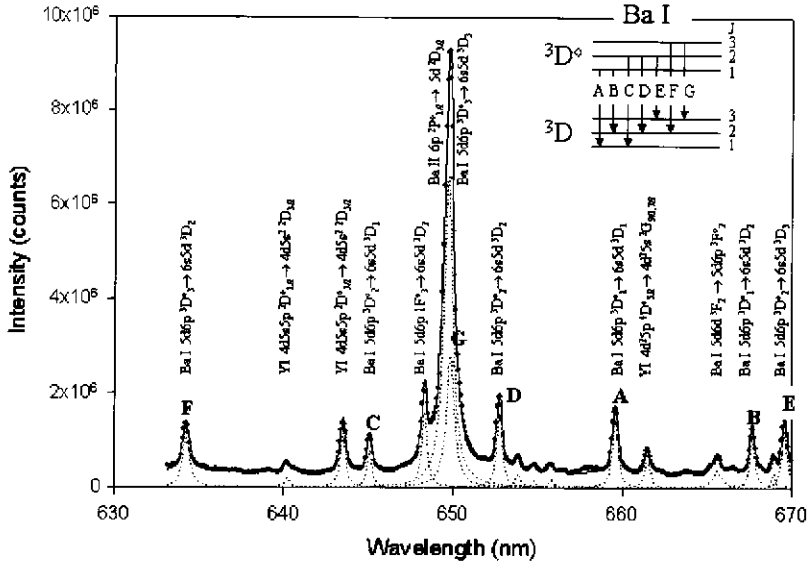


**Fig. 12.** Portion of the visible plume emission spectrum showing the seven components of the BaI 5d6p $^3D^o \rightarrow$ 6s5d $^3D$ fine structure. The spectrum was fitted to a series of Gaussian profiles (. . . .) to determine the relative intensities of the various spectral features.

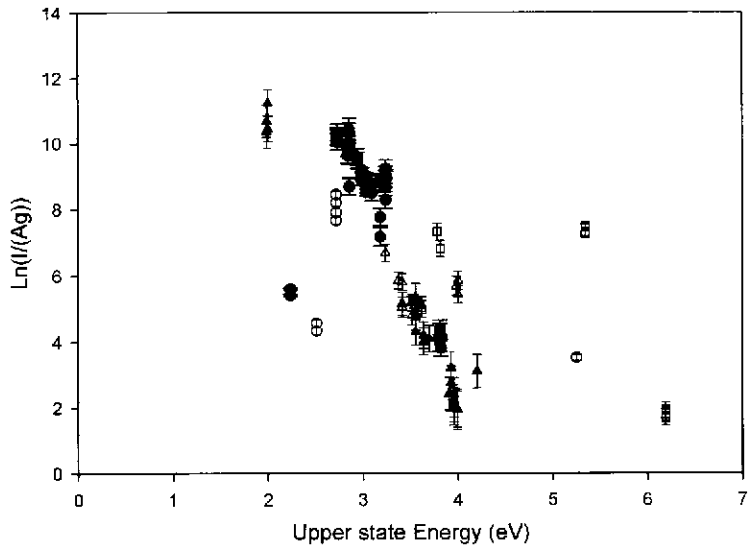


**Fig. 13.** Electronic state distribution, illustrating a common electronic temperature for states unaffected by optical trapping. The lower grouping is associated with transitions terminating on ground states and exhibits considerable optical trapping. Several emitters are included: ♦, Ba I; ◊, Ba II; ▲, Y I; △, Y II; and □, Cu I.

Indeed, many of the emitted intensities are well represented by a single electronic temperature, $T_e$, as shown in Fig. 13. Radiation trapping is significant in these plumes, explaining the second distribution for emission terminating on ground electronic states. Indeed, a Planckian distribution is adequate to describe these highly trapped emissions. The evolution of these temperatures as the plume propagates from the target has been determined and will be the subject of a subsequent paper.

## 4. Conclusions

Plumes generated during the pulsed laser deposition of YBCO are very energetic, with translation and electronic degrees of freedom not in equilibrium. The development of optical diagnostics that are correlated with the quality of deposited films appears quite promising. In particular, the species-dependent angular distributions are strongly correlated with critical current densities of superconducting films and offer a significant complement to process control based on time-of-flight monitoring techniques.

The use of fast imaging sensors to obtain emission TOF profiles during PLD offers several advantages over traditional nonimaging techniques: 1) complete, simultaneous mapping of the spatial evolution of the plume speed distributions, 2) reproducible, well-defined spatial resolution and field of view, 3) convenient implementation on many PLD chambers, and 4) simultaneous recording of additional plume dynamics such as angular distributions and shock dynamics. However, the production of TOF profiles from imagery does require minimal averaging to remove pulse-to-pulse jitter and intensities fluctuations when considered for a real-time feedback mechanism. The resulting TOF profiles compare quit favorably with fixed sensor data. The imagery-based TOF profiles exhibit less intensity in the wings of the profile than the corresponding fixed-point sensors. However, systematic variations in

extracted streaming speeds and temperatures between imaging and nonimaging sensors are smaller than the variations in nonimaging sensors viewing the same plumes.

Significant deviation from the typical modified-Maxwellian speed distributions has been observed, particularly near the target. Extracted streaming speeds and temperatures are strongly dependent on the functional form for the preexponential speed factor. The extension of imaging TOF profiles to process control is promising.

## References

[1]Barnes, P.N., G.L. Rhoads, J.C. Tolliver, M.D. Sumption, and K.W. Schmaeman, "Compact, Lightweight Superconducting Power Generators," presented at the 12th Symposium on Electromagnetic Launch Technology (2004); to appear in IEEE Trans. Mag.

[2]Biggers, R.R., J.G. Jones, I. Maartense, J.D. Busbee, D. Dempsey, D. Liptak, D. Lubbers, C. Varanasi, and D. Mast, Eng. Applic. Artific. Intell. **11**, 627 (1998).

[3]Biggers, R.R., G. Kozolowski, and J. Jones, Integrated Ferroelectrics **28**, 201 (2000).

[4]Christy, D., and G. Hubler, *Pulsed Laser Deposition of Thin Films*, Wiley, New York (1994).

[5]Foltyn, S.R., P.N. Arendt, R.F. DePaula, P.C. Dowden, J.Y. Coulter, J.R. Groves, L.N. Haussamen, L.P. Winston, Q.X. Jia, and M.P. Maley, Physica C **341–348**, 2305 (2000).

[6]Foltyn, S.R., P.N. Arendt, P.C. Dowden, R.F. DePaula, J.R. Groves, J.Y. Coulter, Q.X. Jia, M.P. Maley, and D.E. Peterson, IEEE Trans. Appl. Superconductivity **9**, 1519 (1999).

[7]Fukushima, K., Y. Kanke, and M. Badaye, J. Appl. Phys. **77**, 5406 (1995).

[8]Geohagen, D.B., Thin Solid Films **220**, 138 (1992).

[9]Geohegan, D.B., Appl. Phys. Lett. **60**, 2732 (1992).

[10]Geohagen, D.B., and D.N. Mashburn, Appl. Phys. Lett. **55**, 2345 (1989).

[11]Geohegan, D.B., and D.N. Mashburn, Mater. Res. Soc. Symp. Proc. **191**, 211 (1990).

[12]Kakimoto, K., Y. Iijima, and T. Saitoh, Physica C **392–396**, 783 (2003).

[13]Kelly, R., and R.W. Dreyfus, Surf. Sci. **198**, 263 (1988).

[14]Kools, J.C.S., T.S. Baller, S.T. DeZwart, and J. Dieleman, J. Appl. Phys. **71**, 4547 (1992).

[15]Larbalestier, D., A. Gurevich, M. Feldman, and A. Polyanskii, Nature **414**, 368 (2001).

[16]Li, Y., K. Zdun, J. Hope, J. Xie, S. Corcoran, Y. Qiao, J. Reeves, K. Lenseth, and V. Selvamanickam, IEEE Trans. Appl. Superconductivity **13**, 2758 (2003).

[17]Nakata, Y., H. Kaibara, T. Okada, and M. Maeda, J. Appl. Phys. **80**, 2458 (1996).

[18]Otis, C.E., and P.M. Goodwin, J. Appl. Phys. **73**, 1957 (1993).

[19]Payling, R., and P. Larkins, *Optical Emission Lines of the Elements*, Wiley, New York (2000).

[20]Riley, D., L. Doyle, and R. Al-Wazzan, J. Appl. Phys. **79**, 7223 (1996).

[21]Selvamanickam, V., H.G. Lee, Y. Li, X. Xiong, Y. Qiao, J. Reeves, Y. Xie, A. Knoll, and K. Lenseth, Physica C **392–396**, 859 (2003).

[22]Selvamanickam, V., Y. Li, X. Xiong, Y. Xie, J. Reeves, Y. Qiao, Y. Chen, A. Knoll, T. Salagaj, and K. Lenseth, "Progress in Scale Up of Second-Generation HTS Conductors at SuperPower," Applied Superconductivity Conference, Jacksonville, FL 2004; Iijima, Y., K. Kakimoto, Y. Sutoh, S. Aijimura, and T. Saitoh, "Development of Long Y-123 Coated Conductors for Coil-Applications by IBAD/PLD Method," Applied Superconductivity Conference, Jacksonville, FL (2004).

[23]Singh, R., and D. Kumar, Mater. Sci. Eng.: R Reps **22**, 113 (1998).

[24]Tolliver, J.C., G.L. Rhoads, P.N. Barnes, S.F. Adams, and C.E. Oberly, "Superconducting Generators: Enabling Airborne Directed Energy Weapons," AIAA Paper 2003-5917 (2003).

[25]Zheng, J.P., Z.Q. Huang, and D.T. Shaw, Appl. Phys. Lett. **54**, 280 (1989).

[26]Zheng, R., M. Campbell, K.W.D. Ledingham, W. Jia, C.T.J. Scott, and R.P. Singhal, Spectrochim. Acta Pt. B: At. Spectrosc. **52**, 339 (1997).

## The Authors

**Dr. Paul N. Barnes** received his B.S. degree in Physics from Brigham Young University in 1985, and then later his Ph.D. degree in Physics from the University of Illinois at Urbana–Champaign in 1996. He is currently the Superconductivity Group Leader in the

Propulsion Directorate at the Air Force Research Laboratory as a senior research physicist. Dr. Barnes's research interests include high-temperature superconducting films, ceramic oxides, biaxially textured metals, magnetic flux pinning and ac losses in superconductors, and superconducting power generator applications.

**Dr. Rand R. Biggers** received his B.A. degree in Physics from Knox College in 1968, his M.S. degree in Physics from Northern Illinois University in 1977, and his Ph.D. degree in Physics from Kent State University in 1983. He is currently a Senior Research Physicist in the Materials and Manufacturing Directorate of the Air Force Research Laboratory, serving since 1990. He was previously a Senior Research Physicist at the Naval Coastal Systems Center, Panama City, FL, from 1983 until 1990. Biggers's research interests include process control of pulsed laser deposition, superconductivity, and thermal conductivity control in liquid crystals.

**Mr. Carl J. Druffner** is conducting his Ph.D. research in optical diagnostics of pulsed laser deposition under the direction of Dr. Perram at the Air Force Institute of Technology (AFIT) while pursuing his Ph.D. in Materials Engineering from the University of Dayton (UD). He obtained a B.S. degree in Chemical Engineering in 1995 from UD. He worked as a Research Engineer doing R&D of polymers, pharmaceuticals, and specialty chemicals in industry until 2000. He returned to academia with the UD Research Institute (UDRI) and the Center for Material Diagnostics to complete a M.S. degree in Material Engineering at UD in 2002 dealing with nondestructive evaluation of microelectronic components. He should complete his Ph.D. in late 2005.

**Major Patrick Kee** (M.S., Air Force Institute of Technology, 1994; B.A., University of Nebraska–Omaha, 1989) is the Chief, Electro-Optic Target Detection System, Sensors Directorate, Air Force Research Laboratory (AFRL), and Doctoral Candidate, Air Force Institute of Technology, Wright–Patterson Air Force Base. His dissertation research topic involves measuring energy distributions for species created in the pulsed-laser deposition of superconducting films. His prior technical interests have included plasma deposition of diamond thin films, spectroscopic measurements of weakly ionized plasmas, monitoring of nuclear tests through seismic and analytical laboratory techniques, and electronic warfare applications. In his role at AFRL, he is currently supporting the development and testing of passive electro-optic sensors to support various Department of Defense missions.

**Mr. Matthew Lange** received his B.S. degree in Physics form the University of Akron in 1999 and his M.S. degree in Applied Physics from the Air Force Institute of Technology in 2001. He is currently working to attain his Ph.D. degree in Applied Physics at the Air Force Institute of Technology.

**Dr. Glen P. Perram** received his B.S. degree in Applied Physics from Cornell University in 1980 and his M.S. and Ph.D. degrees in Physics from the Air Force Institute of Technology in 1981 and 1986. He is currently Professor of Physics at the Air Force Institute of Technology, having served as a member of the faculty since 1989. Professor Perram's research interests include chemical lasers, remote sensing, optical diagnostics, and laser weapon systems modeling.